nature chemistry

ARTICLES

PUBLISHED ONLINE: 4 JULY 2010 | DOI: 10.1038/NCHEM.724

Two- and three-dimensional extended solids and metallization of compressed XeF_2

Minseob Kim, Mathew Debessai and Choong-Shik Yoo*

The application of pressure, internal or external, transforms molecular solids into extended solids with more itinerant electrons to soften repulsive interatomic interactions in a tight space. Examples include insulator-to-metal transitions in O_2, Xe and I_2, as well as molecular-to-non-molecular transitions in CO_2 and N_2. Here, we present new discoveries of novel two- and three-dimensional extended non-molecular phases of solid XeF_2 and their metallization. At ~50 GPa, the transparent linear insulating XeF_2 transforms into a reddish two-dimensional graphite-like hexagonal layered structure of semiconducting XeF_4. Above 70 GPa, it further transforms into a black three-dimensional fluorite-like structure of the first observed metallic XeF_8 polyhedron. These simultaneously occurring molecular-to-non-molecular and insulator-to-metal transitions of XeF_2 arise from the pressure-induced delocalization of non-bonded lone-pair electrons to sp^3d^2 hybridization in two-dimensional XeF_4 and to p^3d^5 in three-dimensional XeF_8 through the chemical bonding of all eight valence electrons in Xe and, thereby, fulfilling the octet rule at high pressures.

Noble gases with closed shell structures and high ionization potentials are the most inert of chemical species. However, the heavy noble gases with relatively small ionization potentials, such as Kr, Xe and Rn, can form chemical compounds with electronegative elements, as first realized in $XePtF_6$ (ref. 1). Because of the interesting chemical bonding in $XePtF_6$ (ref. 2), there have been numerous studies, both theoretical and experimental, on noble-gas compounds. These have resulted in discoveries of a range of noble-gas compounds including noble-gas halides and extended linear periodic polymers[3–5]. The most stable and most widely investigated of these compounds are the xenon fluorides, XeF_2, XeF_4 and XeF_6 (refs 6–8).

XeF_2, one of the most stable noble-gas fluoride compounds, is a linear symmetric molecule with a body-centred tetragonal structure ($I4/mmm$, $Z = 2$, phase I)[9]. Three lone-pair electrons in the equatorial plane evenly smear out to a torus ring and form cylindrical symmetry with two Xe–F bonds along the axial direction, resulting in a simple linear structure with high thermal stability[6,10–12]. The nature of bonding in XeF_2 can be described in terms of a three-centred four-electron bonding, two electrons from two F atoms and two from sp^3d hybridized Xe atoms, resulting in a mixture of covalent and ionic characters. The previously noted rather long Xe–F bond distance 2.14 (±0.14) Å is difficult to understand in terms of the lone pair–nucleus attraction model[13]. Because high pressure could force the lone pairs to smear symmetrically around the Xe nucleus, it was predicted that the tetragonal phase transformed into a cubic fluorite (CaF_2, $Fm3m$) structure. However, such a transition has not been observed[14].

XeF_2 can be considered to be a chemically precompressed, elemental molecular alloy of Xe and F_2 (refs 15,16), which may provide insight into metallic fluorine below 130 GPa, the pressure at which Xe is known to metallize[17,18]. Note that, with the exception of rare-gas solids, fluorine and chlorine are the only two elements that have not been transformed to extended phases, either metallic or polymeric, at high pressures, presumably due to their formidably high transition pressures above 500 GPa (refs 15,19,20).

We show that linear molecular XeF_2 is indeed unstable above 40–50 GPa, where it transforms into novel extended phases. With increasing pressure, XeF_2 undergoes a series of structural changes, first transforming into a two-dimensional (2D) graphite-like layer structure at 50 GPa, then further transforming into a three-dimensional (3D) fluorite structure above 70 GPa. In addition, these non-molecular phases go through an electronic insulator-to-metal transition that occurs continuously at pressures over 50–70 GPa. The distinctive yet gradual colour change from transparent below

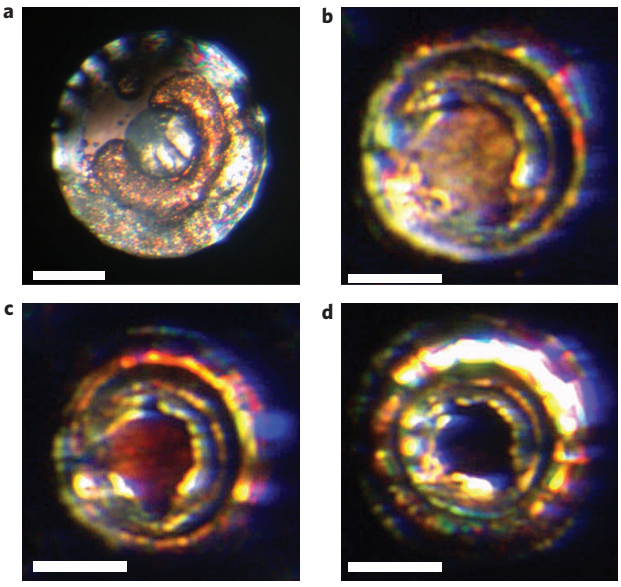

Figure 1 | Micro-photographs of XeF_2 samples at high pressures. **a**, Transparent phase III at 3 GPa, typical for phases I, II, III and IV below 40 GPa. **b**, Yellowish phase IV at 47 GPa. **c**, Reddish phase IV at 53 GPa. **d**, Black phase V at 74 GPa. All images are under transmitted lights. Scale bars: 100 μm (**a**) and 50 μm (**b**–**d**). The sample in **d** is completely opaque and that in **c** is nearly opaque. The samples in **c** and **d** represent the 2D and 3D extended solids, respectively.

Institute for Shock Physics and Department of Chemistry, Washington State University, Pullman, Washington 99164, USA. *e-mail: csyoo@wsu.edu

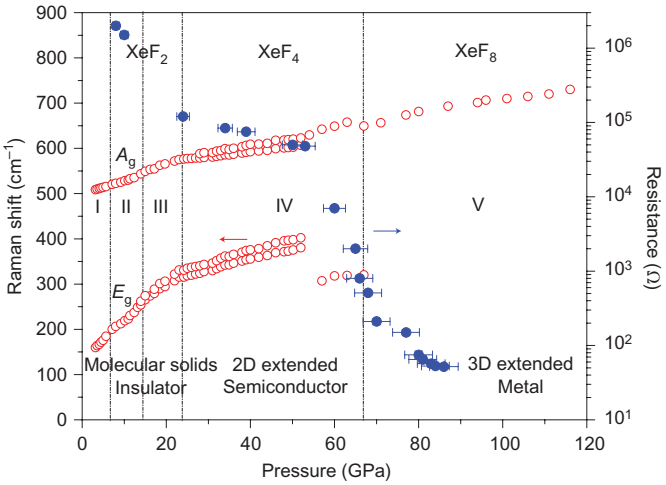

Figure 2 | Pressure dependence of Raman spectra of XeF_2 (open red circles) and electrical resistance (closed blue circles) as a function of pressure. Several phase transitions are marked by dotted lines. The pressure region between 50 and 67 GPa represents the extended nature of the XeF_2 phases and simultaneously includes an insulator-to-semiconductor transition. Note the sudden redshift of ν_1 at ~500 cm^{-1} at 67 GPa, arising from an elongation of the Xe–F bond length at the onset of the phase IV (XeF_4) to V (XeF_8) transition, representing a transition from semiconductor to metal. Details of the Raman spectra are shown in Supplementary Section A.

40 GPa to black above 70 GPa (Fig. 1) is consistent with the observed metallization.

Figure 2 shows the pressure-induced changes in the Raman spectra for XeF_2 as well as resistance changes up to 120 GPa, illustrating the onset of structural and electronic phase transitions. The Raman spectra of XeF_2 below 13 GPa consist of two Raman-active modes: an internal A_g mode for symmetric stretching with ν_1 at 550 cm^{-1} and an external E_g mode for molecular libration at 260 cm^{-1}. Above 13 GPa, the E_g mode splits into two, with a gradual increase in separation to about 22 GPa. Above 22 GPa, there is little change. The A_g mode, on the other hand, remains a singlet below 22–25 GPa, then splits into two with the separation increasing as pressure increases to ~50 GPa. (Details of the Raman spectra are shown to 116 GPa in Supplementary Section A.)

Raman spectral changes above 50 GPa are quite unusual. For example, the E_g libron becomes increasingly weak and almost disappears above 50 GPa. However, a new peak that exists only within a narrow pressure range between 50 and 67 GPa emerges in the lower frequency ~300 cm^{-1} region. The frequency of the A_g ν_1 stretching mode drops abruptly, or redshifts toward a lower frequency at ~67 GPa, above which the peak becomes symmetric in a spectral line shape. These spectral changes are also accompanied by dramatic changes in the electronic structure, which can be noted from changes in the observed resistance: from a typical insulator below 25 GPa, to a semiconductor between 25 and 50 GPa, and finally to a metal above 70 GPa. In this pressure range, the sample also develops distinctive colours. Below 40 GPa the sample is transparent, but it becomes yellow at ~50 GPa, red at ~60 GPa, and black at ~70 GPa (Fig. 1). These changes in colour, Raman spectra and resistance of the sample are reversible following pressure unloading, with a little hysteresis.

The Raman data indicate that XeF_2 undergoes several phase transitions (Fig. 2): to phase II at 7 GPa, signified by the change in the rate of the Raman shift; to phase III at 13 GPa and phase IV at 23 GPa, evident from the splitting of the E_g and A_g modes, respectively; and to phase V at ~70 GPa, indicated by the discontinuous redshift of ν_1. These transitions have also been confirmed by X-ray diffraction measurements (Fig. 3).

Figure 3 plots the observed and calculated powder diffraction patterns of XeF_2 phases to 100 GPa, illustrating the structural evolution from tetragonal (XeF_2–I, $I4/mnm$) to orthorhombic phases (II, *Immm*; III, *Pnnm*–1; IV, *Pnnm*–2; and V, *Fmmm*). The latter two are, respectively, graphite-like 2D (above 50 GPa) and fluorite-like 3D extended solids, as illustrated in Fig. 4. (The refined crystal structures of all phases to 100 GPa are detailed in Supplementary Section B, and their calculated electron density maps are described in Supplementary Section C.) Below 7 GPa, X-ray diffraction patterns are well indexed with a body-centred tetragonal structure ($I4/mmm$). Above 7.0 GPa, the XeF_2 undergoes a tetragonal-to-orthorhombic distortion, evident from the splitting of (101) and (002). The diffraction data between 7 and 15 GPa fit well in terms of *Immm* with F atoms at 4e (0,0,z). The resulting lattice parameters are $a = 3.747(5)$ Å and $b = 3.710(4)$ Å at 9 GPa, with little distortion (<1%) in the a–b plane, induced by intermolecular F...F repulsion resulting from the elongation of Xe–F under anisotropic compression (Fig. 5).

The X-ray diffraction patterns between 15 and 25 GPa can be described either by the same *Immm* structure of phase II or by *Pnnm*–1 with F atoms at 4e (0,0,z). The refined structures of the two alternatives are nearly identical, within 0.1% for all lattice

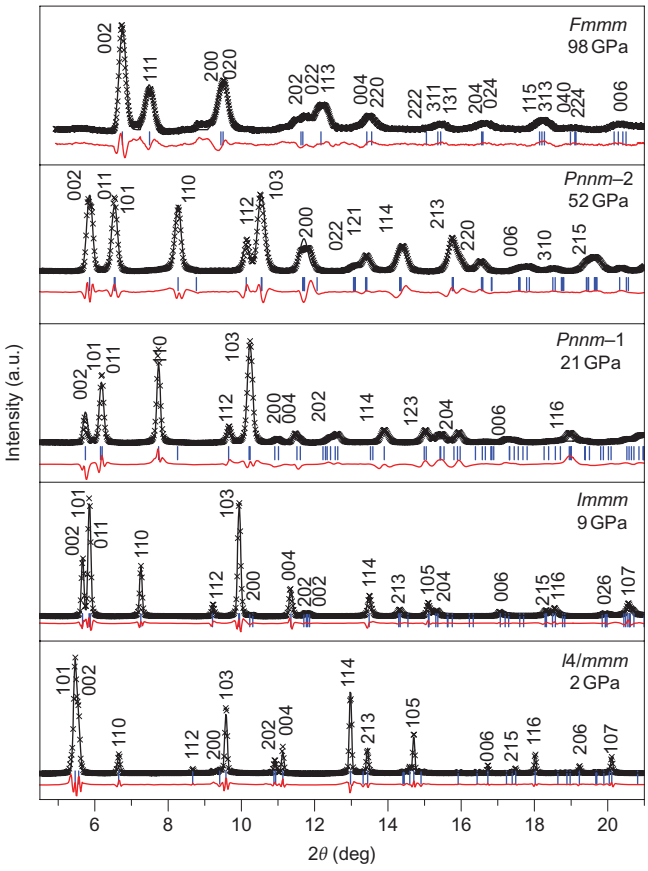

Figure 3 | Angle-resolved X-ray diffraction patterns of XeF_2 phases to ~100 GPa. The red curves are the difference spectra between the observed diffraction data (black crosses) and the refined results (black solid line). Vertical bars mark the positions of Bragg reflections. Only the strong (*hkl*)s are labelled. These structures are based on refinements of the background-corrected diffraction data for lattice parameters, peak profiles, atomic positions and thermal factors, with some preferred orientations on the (103) plane in phase IV and (200) in phase V, both of which represent the layers containing Xe atoms exclusively. The X-ray wavelengths used were 0.3344 Å for the data below 52 GPa and 0.3825 Å for those above 100 GPa. The detailed results are summarized in Supplementary Section B.

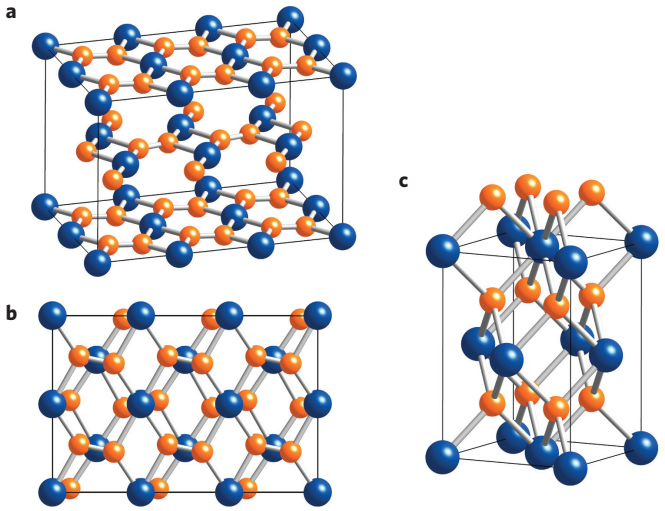

Figure 4 | Crystal structures of graphite-like 2D and fluorite-like 3D extended phases. a, A 2 × 3 × 1 supercell of phase IV in *Pnnm*–2 at 52 GPa. **b**, View along the *c* axis of phase IV, showing the lone-pair electrons of Xe and F roughly overlapping. **c**, Unit cell of the fluorite-like 3D extended phase V in *Fmmm* at 98 GPa. (See Supplementary Section D for computed electron density maps of all phases.) Unit cells are drawn with black lines; Xe and F are in blue and orange, respectively.

parameters: both show the longest intramolecular Xe–F distance, d(Xe–F), at 1.92 Å and the shortest intermolecular d(Xe...F) and d(F...F) at 2.84 and 2.81 Å, respectively. Similarly, the diffraction data between 25 and 52 GPa can be described reasonably well based on the reduced χ^2 (~1.0) value, either by *Pnnm*–2 with F atoms at 4g(x,y,0), or by *Pnnm*–1. However, *Pnnm*–1 fails to match the intensity swap of (002) and (011) peaks above 48 GPa. More importantly, the *Pnnm*–1 results in a continuous increase in d(Xe–F) and a decrease in d(F...F) with pressure and, therefore, dissociation of Xe and F_2 above ~50 GPa. This was not observed, even at 100 GPa. Therefore, *Pnnm*–2 yields the best and physically most meaningful results. *Pnnm*–1 may be a structure that arises in a small range of pressure when XeF_2 transforms from the vertically (along the c axis) aligned *Immm* structure of phase II to the layered (in the a–b plane) *Pnnm*–2 structure of phase IV. Note that the *Pnnm*–2 is isomorphic to β-KrF_2 at −80 °C (ref. 21).

In Fig. 5, the pressure dependence of the XeF_2 phases are shown in terms of the specific volumes (Fig. 5A) and lattice parameters (inset to Fig. 5A) and intra- and intermolecular bond distances (Fig. 5B). The phase I–II transition occurs abruptly with ~4.3% volume collapse at 7 GPa, whereas the II–III–IV transitions occur rather smoothly without any apparent volume changes. Note that solid XeF_2 shows highly anisotropic compressibility along the a (or b) and c axes, resulting in a pseudo-cubic structure (that is, 2 × 2 × 1 supercell) at ~50 GPa where phase IV (*Pnnm*–2) becomes an extended solid as described below.

The pressure dependence of the first (and second) nearest-neighbour distances, XeF1 (XeF2) and FF1, supports the above *Pnnm*–2 model (see Fig. 5B). Note that at ~20 GPa, the fluorine atoms are well separated from each other at d(FF1) = 2.8 Å, which collapses to ~1.3 Å at 52 GPa. This value compares with a typical FF bond distance, 1.41 Å, in solid fluorine at ambient pressure[22]. Although the 7% reduction in the F–F distance is quite reasonable at 52 GPa, the reversible nature of the present Raman, X-ray and resistance results further rule out the possibility of F_2 decomposition. At this point, both XeF1 and XeF2 distances are ~1.9 Å. This is close enough for the formation of covalent bonds between the Xe atom and the two adjacent F atoms, in comparison with the Xe–F bond distance of 2.14 Å at ambient pressure[9]. Therefore, the structure of phase *Pnnm*–2 at 52 GPa should be considered to be an extended layer structure with a layer separation of 3.28 Å (or, c/2), as shown in Fig. 4.

At ~70 GPa, phase IV transforms to yet another extended phase V with an orthorhombic unit cell: *Fmmm* with Xe at 4a(0,0,0) and F at 8f(1/2,1/2,1/2). This is nearly a cubic fluorite-like structure with the lattice parameters a (4.499(3) Å) ≈ b (4.514(2) Å) ≈ $1/\sqrt{2} \times c$ (6.433(2) Å) at 78 GPa. In this phase, the adjacent layers of XeF_4 are interconnected, with four F atoms occupying all eight tetrahedral sites of the *Pnnm*–2 unit cell. Xenon atoms are coordinated with the eight nearest fluorine atoms in XeF_8 polyhedra at a Xe–F bond distance of ~2.3 (±0.1) Å, which is substantially longer than that of XeF_4 in phase IV, ~1.9 (±0.1) Å. Nevertheless, phase V is ~2.0% more dense than phase IV at the transition pressure 70 GPa. Fluorine atoms, on the other hand, are fourfold coordinated with xenon atoms in distorted tetrahedra, indicating sp^3 hybridization in the fluorine atoms. Note that the extremely large compression of XeF_2, at nearly 50% of the ambient volume (Fig. 5), is consistent

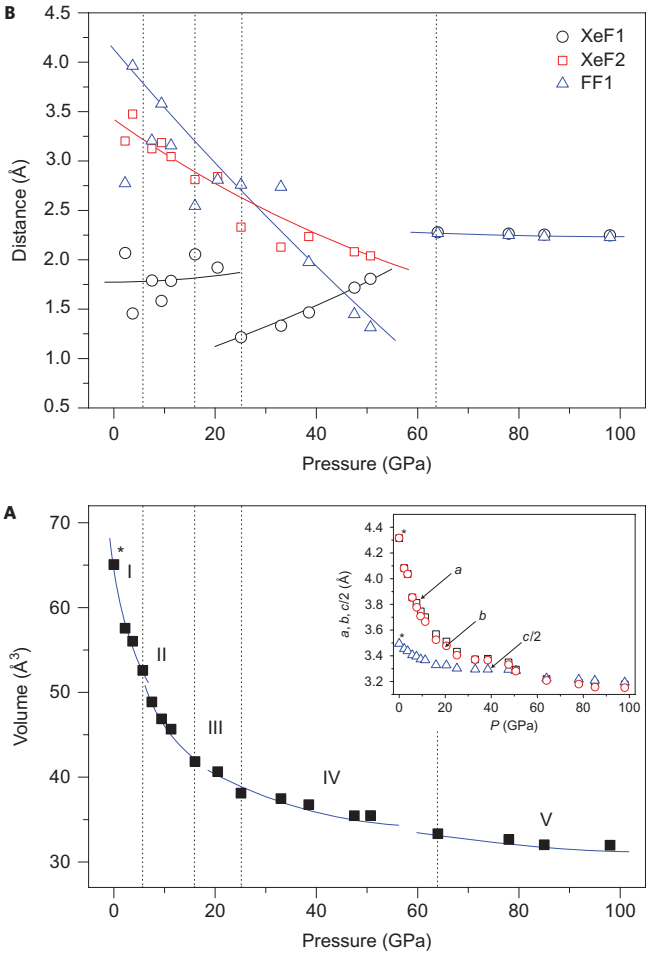

Figure 5 | Pressure dependence of the crystal structure and chemical bonds of the XeF_2 phases. A, Specific volumes and lattice parameters (inset). **B**, Intra- and intermolecular bond distances of XeF_2. XeF1 (XeF2) and FF1 represent the first (second) nearest-neighbour distances of Xe and F atoms, respectively. Note that all bond distances are equal in phase V. The region marked with grey above ~40–50 GPa indicates the extended nature of the XeF_2 phases. Data at ambient pressure (marked by an asterisk) are taken from ref. 9. Note that the inter- (XeF1) and intra- (XeF2) bond distances become nearly equal above 50 GPa, ~1.9 Å in phase IV at ~50 GPa and ~2.3 Å in phase V at ~70 GPa. The sudden increase in the XeF distance at 70 GPa is due to the increase in Xe coordination from XeF_4 in phase IV to XeF_8 in phase V.

with a large increase in the number of nearest neighbours with increasing pressure. The Xe–F–Xe angles are 120° between interlayer Xe atoms (along the *c* axis) and 90° between intralayer Xe atoms (in the *a*–*b* plane), indicating an ionic nature for the Xe–F bonds, which is prone to structural distortion and likely arises from the p^3d^5 hybridization in Xe atoms rather than the sp^3d^5 (ref. 6). At the same density, a perfect isotropic fluorite (*Fm*3*m*) structure would yield a slightly shorter Xe–F bond distance, for example, 2.17 Å instead of the 2.25 Å of phase V at 98 GPa.

The formation of extended solids explains the abovementioned unusual changes in Raman spectra above 50 GPa (Fig. 2). The new low-frequency mode of extended phase IV, for example, is likely the interlayer shearing mode E_{2g}, similar to that of graphite[23]. The redshift of the ν_1 mode at 67 GPa is due to the elongation of the Xe–F bond length across the transition from the 2D (1.9 Å) to 3D (2.3 Å) extended solids. The symmetric Raman lineshape of phase V can be understood in terms of its high-symmetry, fluorite-like structure, which contains only one first-order Raman-active T_g mode. The splittings of the E_g in phase III and ν_1 modes in phase IV represent the factor group or Davydov splittings. The increase in the separation represents the enhanced intermolecular coupling as pressure increases.

The present study demonstrates that linear molecular XeF_2 transforms to novel 2D and 3D extended solids (Fig. 4) through several intermediary phases. The crystal structure of phase III (*Pnnm*–1), for example, can be regarded as an intermediate state between the molecular phase I (*Immm*) and the extended phase IV (*Pnnm*–2), in which the disparity between *d*(Xe–F) and *d*(Xe...F) decreases continuously with increasing pressure. The anisotropic compressibility, substantially greater along the *a* and *b* axes than along the *c* axis, brings the lone-pair electrons of the Xe atoms in the *a*–*b* plane closer to the nucleus and, thus, screens off the effective nuclear charge of Xe from the valence electron. This leads to a reduction of the bond energy and an elongation of the Xe–F bond distance, as observed in Fig. 5. When the pressure reaches ~23 GPa, the F atoms are closer to the Xe atoms in the upper (or lower) layer, converting phase III into a layer structure of phase IV with sudden collapses in F–F and Xe–F distances.

In phase IV, the ratio between *d*(Xe–F) and *d*(Xe...F) decreases continuously from ~2.0 at 21 GPa where XeF_2 molecules are still molecular yet strongly associated, to ~1.2 at 52 GPa where it becomes a 2D graphite-like layer structure of extended six-membered Xe_2F_4 rings (Fig. 4a). In the extended layer structure, each Xe atom is coordinated with four F atoms through sp^3d^2 hybridization, which leaves out two lone-pair electrons along the *c*-axis direction, roughly at the centre of F–F bonds in two adjacent layers. Note that each F atom is coordinated with two Xe atoms and one F atom, leaving two lone-pair electrons at the position roughly overlapping with those of the Xe atoms (Fig. 4b). Such a repulsive interlayer interaction between the lone-pair electrons of Xe and F atoms is responsible for the observed distortion in the hexagons and hexagonal layers of phase IV (see Supplementary Section C). This is the Jahn–Teller or Peierls distortion in solids, which eventually transforms the 2D layer structure to the 3D network and converts non-bonding electrons to bonding near the Fermi level. This model, combined with the pressure-induced band overlap (described in Supplementary Section D) is consistent with the observed insulator-to-metal transition in this pressure range.

In summary, we present the discoveries of novel 2D and 3D extended phases of XeF_2 and their metallization at high pressures, providing fundamental insights into how closed-shell valence electrons of Xe participate in chemical bonding and electronic phase transitions. The 3D structure of phase V is the first example of a rare-gas solid with eightfold coordination polyhedron bonds. These transitions illustrate the following fundamental rules of high-pressure chemistry: (i) increases in electron delocalization from sp^3d in phases I, II and III to sp^3d^2 in phase IV and p^3d^5 in phase V; (ii) increase in the coordination number from 2 to 4 and to 8; (iii) topological packing or densification from a 1D molecular solid to a 2D layer and to a 3D network. Finally, the metallization of XeF_8 was found to occur at 70 GPa, well below that of Xe or F_2.

Methods

XeF_2 is highly reactive with most metals or thin layers of metal oxides at room temperature. We found that XeF_2 reacted with a bare Re gasket below 5 GPa, yielding ReF_4 impurities, as indicated by Raman measurements showing extra peaks at 414, 761, 827 and 1,105 cm^{-1} at 23 GPa. It even reacted with a Au liner gasket at ~12 GPa, evident in both the Raman spectra and as black stains in the sample. In these experiments we therefore used a Cu liner to minimize chemical reactions with the XeF_2. We found no evidence of chemical reactions in the transparent appearance of XeF_2, or in the Raman spectra or X-ray data. All the data reported here were reversible upon pressure up- and downloadings, confirming that XeF_2 remained unreacted.

Solid XeF_2 (99.99%, Aldrich) was loaded into a membrane diamond anvil cell (DAC). Two Cu-lined Re gaskets with 300- and 100-μm culet diamonds were prepared for low pressures below 50 GPa and high pressures above 50–120 GPa region, respectively. No pressure medium was used. A micrometre-sized ruby chip was loaded into the cell for pressure measurements. Raman spectra of XeF_2 were obtained at room temperature using a confocal micro-Raman system, built in-house, and an Ar^+ laser at 514.5 nm.

The d.c. electrical resistance of XeF_2 was measured at ambient temperature in a DAC with a 300-μm culet using 5-μm-thick copper electrodes. A fine alumina powder mixed with epoxy was used as an electrical insulation layer between the electrodes and the Re gasket. A 100-μm-hole sample chamber was drilled at the centre of the insulation powder. The sample, together with a few ruby chips, was loaded into the sample chamber. From Raman measurements, no extra peaks other than from the sample were found, indicating that there was no chemical reaction between the sample and the alumina powder or with the copper electrode. The four-point resistance method was used, with an average distance between opposing electrodes of ~75 μm. A 1-μA d.c. current was applied using a Lakeshore 120 d.c. current source with switching polarity, and the voltage was measured using a Keithley 2000 DVM. The electrode configuration at 10 GPa pressure is shown in Supplementary Fig. S4. According to most reported high-pressure data[14,24–27], materials with resistance values greater than 1×10^5 Ω are categorized as insulators, for values between 1×10^4 and 1×10^3 Ω as semiconductors, and below 200 Ω are considered to be metals.

Angle-resolved X-ray diffraction (ADXD) data were collected at room temperature using the micro-focused (~10 μm) monochromatic synchrotron X-ray system at 13IDD/GSECARS (λ = 0.3344 Å) and 16BMD/HPCAT (λ = 0.3825 Å) at the Advanced Photon Source. The diffraction patterns were recorded on high-resolution 2D image plates, and Debye–Scherrer diffraction images were converted to 1D profiles using the Fit2D program. Rietveld refinement was then performed to determine the crystal structure using a GSAS program.

Received 13 July 2009; accepted 20 May 2010;
published online 4 July 2010

References

1. Bartlett, N. Xenon hexafluoroplatinate(v) $Xe^+[PtF_6]^-$. *Proc. Chem. Soc.* 218 (1962).
2. Graham, L., Graudejus, O., Jha, N. K. & Bartlett, N. Concerning the nature of $XePtF_6$. *Coord. Chem. Rev.* **197,** 321–334 (2000).
3. Grochala, W. Atypical compounds of gases, which have been called 'noble'. *Chem. Soc. Rev.* **36,** 1632–1655 (2007).
4. Tramsek, M. & Zemva, B. Synthesis, properties and chemistry of xenon(II) fluoride. *Acta Chim. Slov.* **53,** 105–116 (2006).
5. Brown, E. C., Cohen, A. & Gerber, R. Prediction of a linear polymer made of xenon and carbon. *J. Chem. Phys.* **122,** 171101 (2005).
6. Pauling, L. Angles between orthogonal *spd* bond orbitals with maximum strength. *Proc. Natl Acad. Sci.* **73,** 1403–1405 (1976).
7. Dixon, D. A., de Jong, W. A., Peterson, K. A., Christe, K. O. & Schrobilgen, G. J. Heats of formation of xenon fluorides and the fluxionality of XeF_6 from high level electronic structure calculations. *J. Am. Chem. Soc.* **127,** 8627–8634 (2005).
8. Jortner, J., Rice, S. A. & Wilson, E. G. Speculation concerning the nature of binding in xenon fluorine compounds. *J. Chem. Phys.* **38,** 2302–2303 (1963).
9. Agron, P. A. *et al.* F. Xenon difluoride and the nature of the xenon–fluorine bond. *Science* **139,** 842–844 (1963).
10. Grochala, W., Hoffmann, R., Feng, J. & Ashcroft, N. W. The chemical imagination at work in *very* tight places. *Angew. Chem. Int. Ed.* **46,** 3620–3642 (2007).
11. Sidgwick, N. V. & Powell, H. M. Bakerian lecture. Stereochemical types and valency groups. *Proc. R. Soc. Lond. A* **176,** 153–180 (1940).

12. Gillespie, R. J. & Nyholm, R. S. Inorganic stereochemistry. *Q. Rev. Chem. Soc.* **11,** 339–380 (1957).
13. Andersson, S. On the stereochemistry of valence bonds and the structures of XeO_3, XeF_4 and XeF_2. *Acta Cryst.* **B35,** 1321–1324 (1979).
14. Schwarz, U. & Syassen, K. The behavior of solid XeF_2 under pressure. *High Pressure Res.* **9,** 47–50 (1992).
15. Ashcroft, N. W. Hydrogen dominant metallic alloys: high temperature superconductors? *Phys. Rev. Lett.* **92,** 187002 (2004).
16. Eremets, M. I., Triojan, I. A., Medvedev, S. A., Tse, J. S. & Yao, Y. Superconductivity in hydrogen dominant materials: silane. *Science* **319,** 1506–1509 (2008).
17. Reichlin, R. *et al.* Evidence for the insulator–metal transition in xenon from optical, X-ray and band-structure studies to 170 GPa. *Phys. Rev. Lett.* **62,** 669–672 (1989).
18. Goettel, K. A., Eggert, J. H., Silvera, I. F. & Moss, W. C. Optical evidence for the matallization of xenon at 132(5) GPa. *Phys. Rev. Lett.* **62,** 665–668 (1989).
19. Takemura, K., Sato, K., Fujihisa, H. & Onoda, M. Modulated structure of solid iodine during its molecular dissociation under high pressure. *Nature* **423,** 971–974 (2003).
20. Fujihisa, H., Fujii, Y., Takemura, K. & Shimomura, O. Structural aspects of dense solid halogens under high pressure studied by X-ray diffraction—molecular dissociation and metallization. *J. Phys. Chem. Solids* **56,** 1439–1444 (1995).
21. Burbank, R. D., Falconer, W. E. & Sunder, W. A. Crystal structure of krypton difluoride at −80 °C. *Science* **178,** 1285–1286 (1972).
22. Robinson, E. A., Johnson, S. A., Tang, T.-H. & Gillespie, R. J. Reinterpretation of the lengths of bonds to fluorine in terms of an almost ionic model. *Inorg. Chem.* **36,** 3022–3030 (1997).
23. Reich, S. & Thomsen, C. Raman spectroscopy of graphite. *Phil. Trans. R. Soc. Lond. A* **362,** 2271–2288 (2004).
24. Eremets, M. I. *et al.* Superconductivity of Xe at Mbar pressure. *Phys. Rev. Lett.* **85,** 2797–2800 (2000).
25. Eremets, M. I., Struzhkin, V. V., Mao, H. K. & Hemley, R. J. Superconductivity in boron. *Science* **293,** 272–274 (2001).
26. Shimizu, K., Ishikawa, H., Takao, D., Yagi, T. & Amaya, K. Superconductivity in compresed Li at 20 K. *Nature* **419,** 597–599 (2002).
27. Qazilbash, M. M. *et al.* Mott transition in VO_2 revealed by infrared spectroscopy and nano-image. *Science* **318,** 1750–1553 (2007).

Acknowledgements

Synchrotron X-ray diffraction studies were carried out at the GSECAR 13IDD and HPCAT 16BMD beam line at the Advanced Photon Source. The authors thank P. Dera, V. Prakapenka, O. Shebanova and A. Sengupta for their technical support. The present study was supported by DTRA (grant no. HDTRA1-09-1-0041), NSF-DMR (grant no. 0854618) and DOE-NNSA (no. DE-F603-97SF21388).

Author contributions

M.K. carried out X-ray and Raman measurements and performed the analysis, including calculating the electronic structure. M.D. performed resistance measurements and analysis. C.-S.Y. was responsible for the overall design, direction and supervision of the project. All authors contributed to writing of the manuscript.

Additional information

The authors declare no competing financial interests. Supplementary information accompanies this paper at www.nature.com/naturechemistry. Reprints and permission information is available online at http://npg.nature.com/reprintsandpermissions/. Correspondence and requests for materials should be addressed to C.S.Y.